ARTICLE

Ionic Liquid Pretreatment of Poplar Wood at Room Temperature: Swelling and Incorporation of Nanoparticles

Marcel Lucas,* Brian A. Macdonald, Gregory L. Wagner, Stephen A. Joyce, and Kirk D. Rector*

Chemistry Division, Los Alamos National Laboratory, Los Alamos, New Mexico 87545

ABSTRACT Lignocellulosic biomass offers economic and environmental advantages over corn starch for biofuels production. However, its fractionation currently requires energy-intensive pretreatments, due to the lignin chemical resistance and complex cell wall structure. Recently, ionic liquids have been used to dissolve biomass at high temperatures. In this study, thin sections of poplar wood were swollen by ionic liquid (1-ethyl-3-methylimidazolium acetate) pretreatment at room temperature. The samples contract when rinsed with deionized water. The controlled expansion and contraction of the wood structure can be used to incorporate enzymes and catalysts deep into the wood structure for improved pretreatments and accelerated cellulose hydrolysis. As a proof of concept, silver and gold nanoparticles of diameters ranging from 20 to 100 nm were incorporated at depths up to 4 μm. Confocal surface-enhanced Raman images at different depths show that a significant number of nanoparticles were incorporated into the pretreated sample, and they remained on the samples after rinsing. Quantitative X-ray fluorescence microanalyses indicate that the majority of nanoparticle incorporation occurs after an ionic liquid pretreatment of less than 1 h. In addition to improved pretreatments, the incorporation of materials and chemicals into wood and paper products enables isotope tracing, development of new sensing, and imaging capabilities.

KEYWORDS: ionic liquid • wood • pretreatment • lignocellulosic biomass • biofuel

INTRODUCTION

Lignocellulosic biomass represents a potentially sustainable source of liquid fuels and commodity chemicals. It could satisfy the energy needs for transportation and electricity generation, while contributing substantially to carbon sequestration and limiting the accumulation of greenhouse gases in the atmosphere. Potential feedstocks are abundant and include crops (corn, sugar cane), agricultural wastes, forest products, grasses, and algae (1, 2). Among those feedstocks, wood has been so far widely used for the production of paper, as construction material or solid fuel. Wood is mainly constituted of three components: cellulose, hemicellulose, and lignin, which is an amorphous network of cross-linked phenylpropanoid units (3). The conversion process of lignocellulosic biomass typically consists of three steps: (1) pretreatment; (2) hydrolysis of cellulose and hemicellulose into fermentable sugars; and (3) fermentation of the sugars into liquid fuels (ethanol) and other commodity chemicals. The pretreatment step is necessary because of the complex structure of the plant cell wall and the chemical resistance of lignin, which limits the access of enzymes to cellulose. The ideal pretreatment should break the lignocellulosic complex, increase the active surface area, and decrease the cellulose crystallinity, while limiting the generation of inhibitory byproducts and minimizing hazardous wastes and wastewater.

* Corresponding author. E-mail: mlucas@lanl.gov (M.L.); kdr@lanl.gov (K.D.R.).

Received for review April 27, 2010 and accepted June 30, 2010

DOI: 10.1021/am100371q

Current pretreatments, including acid hydrolysis, steam explosion, alkaline hydrolysis, and ammonia fiber explosion, have major drawbacks limiting their application at an industrial scale. The acids used in acid hydrolysis are toxic and necessitate expensive reactors that are resistant to corrosion. For optimal efficiency, the inhibitory byproducts generated during acid hydrolysis have to be removed with activated carbon (4). Hydrolysis with concentrated acids requires a recycling process to make the pretreatment economically viable (5). Considerable amounts of sugars are lost during the neutralization process (6). In the steam explosion process, the major disadvantages are the intense energy consumption and the generation of inhibitory byproducts. The addition of acids or carbon dioxide can reduce the generation of inhibitory byproducts, but increases the overall cost and environmental risks (7). Alkaline hydrolysis requires several days for delignification and has proven more efficient on agricultural wastes than hardwoods with high lignin content (8). Neutralization of the hydrolysate and recovery of the alkali are necessary to reduce the financial and environmental impact. Finally, in the ammonia fiber explosion process, high capital and operative costs are needed to obtain, heat, compress and recover the ammonia (1). Pretreatment represents the most expensive single step in the conversion of lignocellulosic biomass to ethanol, and can cost up to 20% of the total projected cost (1, 2). So it is imperative to develop new pretreatments that are economically viable and environmentally friendly.

Recently, ionic liquids have attracted considerable interest because of their ability to dissolve biopolymers, such as cellulose (9–13), lignin (13–15), native switchgrass (16), and

Published on Web 07/15/2010

wood (saw dust ground from spruce, pine, and oak) (3, 13, 17–19). Ionic liquids are molten salts with a glass transition or melting temperature below 100 °C. They are generally characterized by a high thermal stability and extremely low vapor pressure (13). The long list of possible anion−cation combinations enables the synthesis of ionic liquids with tailored physical properties, such as melting temperature, density, electrical and thermal conductivity (9). Ionic liquids are also considered green solvents, because they have been successfully recycled at high yields for further use with limited efficiency loss. In a typical recycling process, the cellulose-rich wood extracts would first be precipitated with water or acetone/water solution and filtered out. The lignin and other extracts would then be removed with multiple washing and solvent evaporation (13, 17). Regenerated cellulose from ionic liquid solutions of wood can also have a lower degree of polymerization and crystallinity, which facilitate its hydrolysis (9–11, 13). The degradation of cellulose is limited with the use of imidazolium-based ionic liquids, compared to the more damaging pretreatments mentioned earlier. The main dissolution mechanism involved is the disruption of the hydrogen bonding network in cellulose (20). The potential of ionic liquids being used in an industrial process was further increased by the fact that a few microbial cellulases remain active at high ionic liquid concentration (about 30%) (21). However, all studies on the dissolution of wood in ionic liquids have been conducted so far at high temperatures, typically above 90 °C. Development of alternative pretreatments at room temperature is desirable to eliminate the additional energy cost.

In this study, thin sections of poplar wood were swollen at room temperature by a 3 h ionic liquid (1-ethyl-3-methylimidazolium acetate or EMIMAc) pretreatment. The samples contract when rinsed with deionized water. The controlled expansion and contraction of the wood structure can be used to incorporate enzymes and catalysts deep into the wood structure for improved pretreatments and accelerated cellulose hydrolysis. A deeper penetration of enzymes and catalysts offers several benefits: less stringent size reduction requirements for the feedstock (22, 23), reduction of the enzyme loadings, and increase in the solid content in the reactor, which reduces energy and water use, liquid waste, and the reactor volume. As a proof of concept, silver and gold nanoparticles of diameters ranging from 20 to 100 nm were incorporated. This size range is much larger that the size of enzymes and catalysts currently used for the degradation of lignin. Near-infrared confocal surface-enhanced Raman images allowed us to locate gold nanoparticles of 100 nm diameter in the cell walls in three dimensions and assess their density on the sample. Raman spectroscopy has provided valuable information on the spatial distribution of lignin and cellulose in cell walls (24, 25), phase transition in cellulose (26), chemical modification, orientation of the molecules, and mechanical stress (25). Here, the deposition of gold nanoparticles induces a significant enhancement of the Raman signal from the wood in their close proximity, an enhancement attributed to the surface-enhanced Raman effect (SERS) (27). After rinsing with water, scanning electron microscopy (SEM) and Raman images of the same areas show that most nanoparticles remained on the pretreated sample. Raman images at different depths reveal that a significant number of nanoparticles were incorporated into the wood sample, at depths up to 4 μm, or 40 times the diameter of the nanoparticles. Control experiments on an untreated wood sample resulted in the deposition of nanoparticles only at the surface and most nanoparticles were removed upon rinsing. Quantitative X-ray fluorescence microanalyses of particle incorporation as a function of exposure time, normalized to poplar mass, indicate that the majority of nanoparticle incorporation occurs after an ionic liquid pretreatment of less than 1 h. This materials/chemicals incorporation process based on the swelling/contraction of the wood and the disruption of its hydrogen-bond network can be implemented at room temperature, which eliminates a major energy cost and reduces the initial capital investment in future plants. In addition to improved pretreatments, the incorporation of materials and chemicals into wood and paper products enables isotope tracing, catalysis (28), imaging agents (29), drug-delivery systems (30), energy-storage devices (28, 31), and chemical sensors (28, 32).

EXPERIMENTAL SECTION

Materials. Transverse sections of poplar wood (*Populus tremuloides*) of 30 and 40 μm thickness were prepared using a sliding microtome. The sections were dried in an oven for 4 h between two glass slides at 60 °C to prevent curling. The ionic liquid, 1-ethyl-3-methylimidazolium acetate (EMIMAc), was purchased from Sigma-Aldrich (St. Louis, Missouri). Suspensions of 20 nm silver, 60 nm silver, 40 nm gold, and 100 nm gold nanoparticles were purchased from BBInternational, Cardiff, United Kingdom.

Sample Preparation. Two wood samples, ~5 × 5 mm^2, were cut from the same microtome section of 30 μm thickness. One sample was immersed in EMIMAc for 3 h at room temperature. After the EMIMAc pretreatment, the wood sample was blotted with a Kimwipe. The samples were placed on glass coverslips and 5 mL of gold nanoparticles suspension was then deposited on the untreated sample and the pretreated sample. The samples were left to dry overnight in air and then placed between glass coverslips for Raman imaging. After the Raman images, the samples were rinsed with deionized water, left to dry overnight in air and placed between new glass coverslips for further examination. Additionally, rectangular poplar samples were cut from 40 μm thick microtome sections. These samples were pretreated with EMIMAc and exposed to a suspension of 20 nm silver nanoparticles for various amounts of time. After rinsing with water, sections were dried in an oven for 4 h between two glass slides at 60 °C, their uptake of silver nanoparticles was then analyzed by X-ray fluorescence microspectroscopy.

Raman Microscopy. The excitation for the Raman images was the 776 nm laser line of a tunable Ti:Sapphire laser (Mira 900-P, Coherent, Palo Alto, CA) coupled with a 532 nm solid state laser (Millenia VIIIs, Spectra-Physics, Mountain View, CA). The incident laser was filtered spectrally by a short-pass filter at 785 nm (RazorEdge SP01−785RU-25, Semrock, Rochester, NY). The collimated beam was focused to a line using a plano-convex BK 7 150 mm focal length cylindrical lens (CKX150AR.16, Newport Corp., Irvine, CA) and was then redirected to the back of an inverted microscope (Carl Zeiss Axiovert 200, Göttingen, Germany) by a Raman edge dichroic (z785rdc,

Chroma Technology, Rockingham, VT). Spatial coordinates with a submicrometer accuracy from the microscope stage (MS2000XY stage, Applied Scientific Instrumentation Inc., Eugene, OR) and bright-field images at different magnifications from an InfinityX-32camera (Lumenera Corp., Ottawa, Canada) ensured the accurate registry required for the capture of Raman and SEM images at the same area after any sample preparation step. A C-apochromat 63× (N.A. 1.2) water immersion objective (Carl Zeiss) focused the laser line to a line approximately 1 μm wide and 100 μm long on the sample, with a total power of 80 mW at the sample.

The Raman signal was collected in a backscattering configuration through the same objective and dichroic. The signal was focused with a 150 mm spherical lens onto a 50 μm wide slit at the entrance of a Holospec f/2.2 spectrograph (Kaiser Optical Systems, Ann Arbor, MI) and filtered with a Holographic Super-Notch-Plus Filter (HSPF-785.0AR-2.0, Kaiser Optical Systems, Ann Arbor, MI). The signal was then dispersed with a holographic grating (HSG-785-LF, Kaiser) and imaged with a liquid nitrogen-cooled CCD camera (LN/CCD-1024E, Princeton Instruments, Trenton, NJ). The CCD camera recorded spectral information along the horizontal direction and spatial information along the vertical direction. The spectrometer was calibrated spectrally with 4-acetamidophenol, and spatially using lines in the seventh group of a USAF-1951 resolution test target. Custom-written Labview code (National Instruments, Austin, TX) enabled the acquisition of images and their correction for CCD bias voltage, spherical aberrations using the lines of a Kr lamp (Newport Corp., Irvine, CA), and for the nonuniform power along the focused laser line using a NIST relative Raman intensity correction standard (NIST SRM 2241). The Raman images were acquired by moving the sample across the laser line by 0.5 μm steps. The exposure time for each line was 2 min.

For the collection of Raman images at different depths, an additional pinhole was added before the spectrograph to reduce out-of-focus signals from the sample. The pinhole aperture diameter was decreased to reduce the Raman signal by a factor of 10. Since the signal is focused on a slit at the entrance of the spectrograph, the spatial resolution remains higher along the horizontal direction of the CCD camera than along the vertical direction. The objective was moved along the depth direction by 2 μm steps. The exposure time for the Raman images at different depths was 30 s for each line.

Data Analysis. The data analysis was performed using custom-written Labview code. Each CCD image corresponds to the signal from a line on the sample, and consists of 256 spectra collected at regular spatial intervals along that line. Each spectrum was integrated from 1050 to 1140 cm^{-1} to form one line of the resulting Raman image. Apart from the CCD bias voltage, no other background from the sample was removed from the data. For the Raman intensity depth profile of hot spots, the intensity of all pixels in a 2 × 2 μm^2 area (total of 4 × 8 pixels, the size of the pixel is 0.50 × 0.26 μm^2) around each spot was integrated for each image at a particular depth. To normalize the intensity depth profile of each spot, its minimum value was subtracted from it and it was then divided by its maximum value. The error bars represent the uncertainty on the position of the selected 2 × 2 μm^2 area around the hot spot.

Laser Scanning Fluorescence Microscopy. Autofluorescence images of poplar wood sections were collected with a Zeiss LSM 510 confocal system mounted on a Zeiss Axiovert 200 M inverted microscope. A 514 nm argon ion laser was used as excitation and the fluorescence signal was collected with the Meta detector over a 600−620 nm range with a 63× oil objective (NA 1.4).

Scanning Electron Microscopy. Scanning electron micrographs were acquired using a FEI Quanta 200FEG operating at an accelerating voltage of 30 kV with a backscatter detector. Samples were mounted on one of the glass coverslips used during Raman imaging.

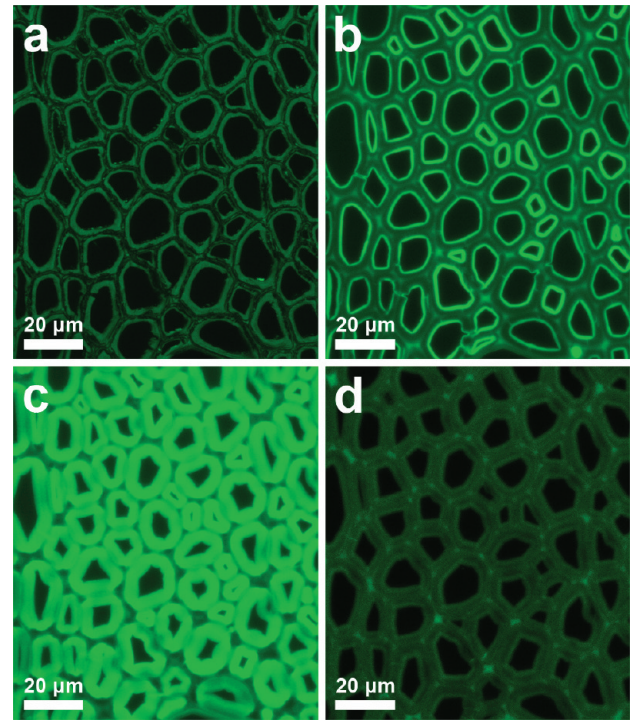

FIGURE 1. Autofluorescence images of poplar wood cells (a) before ionic liquid pretreatment, (b) 15 min into the pretreatment, (c) after 3 h pretreatment, and (d) 20 min after rinsing with deionized water. All images were collected in the same conditions. The brightness was increased for image d for clarity.

X-ray Fluorescence Microspectroscopy. An Edax Eagle III energy-dispersive X-ray fluorescence (XRF) microscope was used to quantify nanoparticle uptake by averaging fluorescence over areas of diameter 40−160 μm. The instrument uses an Rh source using settings of 40 kV accelerating voltage, 800 μA current, and 50 μs dwell time to sample the poplar samples. With this configuration, only elements with atomic numbers greater than 11 (Na) are detected. In a typical poplar spectrum, several elements are present including S, K, Ca, P, Mn. The presence of elements S, K, Ca, P, Mn has been previously reported in Aspen ash (33). The calcium content is heterogeneous. The signal from phosphorus is weak, but detectable. There is also some in situ Si content, with likely contamination arising from pressing the poplar sections between glass slides during drying. In addition, Cr, Fe, Ni, Cu are detected, likely present as residue particulates from the microtome blade. In a comparison of total count mapping and elemental mapping, it was determined that K, Mn, and S are the most closely related to both the density and mass of the poplar sample and appear to be homogeneous with material thickness or density. Sulfur concentration (2.30 keV) was selected as an indicator of poplar density as it is most isolated from other spectral signatures. The determination of S and Ag (22.1 keV) concentrations was performed using a corrective baseline average algorithm. The only additional element detected after introduction of EMIMAc in the poplar samples was bromine, which was removed after rinsing with water.

RESULTS AND DISCUSSION

The pretreatment of poplar wood cells by EMIMAc was monitored by a series of autofluorescence images (Figure 1). After a 3 h EMIMAc pretreatment, the cell walls were found

swollen and the cell lumens were reduced. This behavior is in agreement with the expansion of switchgrass cells upon EMIMAc exposure (16). The secondary cell wall layer, in particular the S2 layer, is much more swollen than the areas around the middle lamella. As for the rays and vessels (not shown), they are similar to the areas around the middle lamella: limited increase in fluorescence intensity and volume during the ionic liquid pretreatment. The overall intensity increase is attributed to the introduction of the strongly autofluorescent EMIMAc. To investigate the origin of the autofluorescence signal, we collected emission spectra from a film of crystalline cellulose I and a droplet of EMIMAc with the same laser scanning fluorescence microscope. Emission spectra with excitations at 458, 488, and 514 nm from the poplar samples confirm that the autofluorescence around the cell lumen before the pretreatment (Figure 1a) is from cellulose, whereas the bright autofluorescence around the lumen during the pretreatment (Figure 1b,c) is from EMIMAc (data not shown). The brighter areas around the lumen during the pretreatment might indicate a higher EMIMAc affinity to specific secondary cell wall layers rich in cellulose (24). Cross-sectional area measurements of poplar wood cells found that after the 3 h EMIMAc pretreatment, the cell wall areas increased by 60−100% and the lumen areas were reduced by 40−83%, depending on the original cell size in the dry wood (Figure 1a,c). After the pretreatment, a gentle rinsing with deionized water led to the almost immediate reopening of the lumen (Figure 1d). The cell walls also contracted after rinsing with water, but at a slower pace. Nineteen hours after rinsing, cells walls were still 40−80% larger than their original sizes. Lumen areas recovered 75−85% of their initial values. In contrast, the deposition of deionized water droplets on untreated poplar wood resulted only in a limited expansion of the wood, and the wood cells recovered their original sizes within 30 min after the water evaporated.

The expansion of wood cells by an EMIMAc pretreatment and their subsequent contraction with water rinsing are the basis of a process to incorporate nanoparticles, and potentially other materials/chemicals, into the wood structure. To this effect, the water rinsing was replaced by the exposure of the EMIMAc-pretreated sample to an aqueous suspension of nanoparticles. As the incorporation of silver or gold nanoparticles into the poplar substrate is inhomogeneous even at the 100 μm distance scale, microscopic analyses alone are insufficient to quantify nanoparticle uptake. Therefore, XRF microspectroscopy was employed to quantify uptake and to test experimental conditions to maximize uptake. Experiments were conducted by varying the exposure time to EMIMAc (up to 4 h) followed by separate, fixed exposure to a suspension of silver nanoparticles (1 or 4 h). These data are reported in Table 1, to an error within 10%. As a negative control, the poplar sample was exposed to the silver suspension for one or four hours without EMIMAc pretreatment and rinsed to test for the possibility of silver mechanical or electrostatic association. The XRF measurements indicated silver presence in the control samples at the instrument detection limit, with slightly more silver present when exposed for longer time, as might be expected. This is in agreement with the data shown in Figure 2 without EMIMAc pretreatment. In all experiments measured, exposure to both EMIMAc and silver suspension resulted in at least an order of magnitude increase in the particle incorporation, again in rough agreement with the microscopy data shown in Figure 2. The data suggest that exposure to EMIMAc or silver suspension longer than 1 h has only a subsequently minor, increasing influence on particle incorporation. Further, increased exposure to silver has a negligible or minor influence to particle incorporation at these time scales.

Table 1. Incorporation of 20 nm Silver Nanoparticles into Microtomed Poplar Substrates As a Function of EMIMAc Exposure from 0 to 4 h for either 1 or 4 h Subsequent Exposure to Silver Nanoparticles Suspension

EMIMAc time (h)	Ag time (h)	Ag/S K ratio
0	1	0.0016
1	1	0.02
2	1	0.022
0	4	0.0052
2	4	0.019
4	4	0.032

For the microscopy experiments, thin sections of poplar were pretreated for 3 h with EMIMAc, and then exposed to a suspension of 100 nm gold nanoparticles. As a control experiment, an untreated poplar wood section was also exposed to the same suspension of nanoparticles. After the deposition of 100 nm gold nanoparticles, three Raman images were collected at different areas from the untreated sample and the one pretreated with EMIMAc (Figure 2, top row). In addition to the cellulose Raman signal, which reveals the wood cell walls, there are multiple hot spots (shown as white spots) attributed to the presence of gold nanoparticles or aggregates of nanoparticles. The Raman signal at these hot spots is significantly enhanced because of the field enhancement in close proximity of gold nanoparticles (27). The significant enhancement, which reaches 2 orders of magnitude for some hot spots, indicates that the laser excitation energy is close to the surface plasmon resonance of these nanoparticles of 100 nm diameter, or clusters of these nanoparticles. Using the same excitation, no noticeable enhancement was observed from 20 nm diameter silver nanoparticles deposited on wood, whereas only a small enhancement was observed for 60 nm silver and 40 nm gold nanoparticles. Therefore, only the 100 nm gold nanoparticles will be dealt with in the following discussion. All presented Raman images were obtained by integrating Raman spectra from 1050 to 1140 cm^{-1}, a band that includes the cellulose peaks typically located around 1095 and 1120 cm^{-1} in spontaneous Raman spectra (not enhanced by gold nanoparticles) (27). These two cellulose bands are enhanced by a variable factor depending on the hot spot. Also, the 1095 cm^{-1} band can be shifted to another position from 1081 to 1099 cm^{-1}, whereas the position of

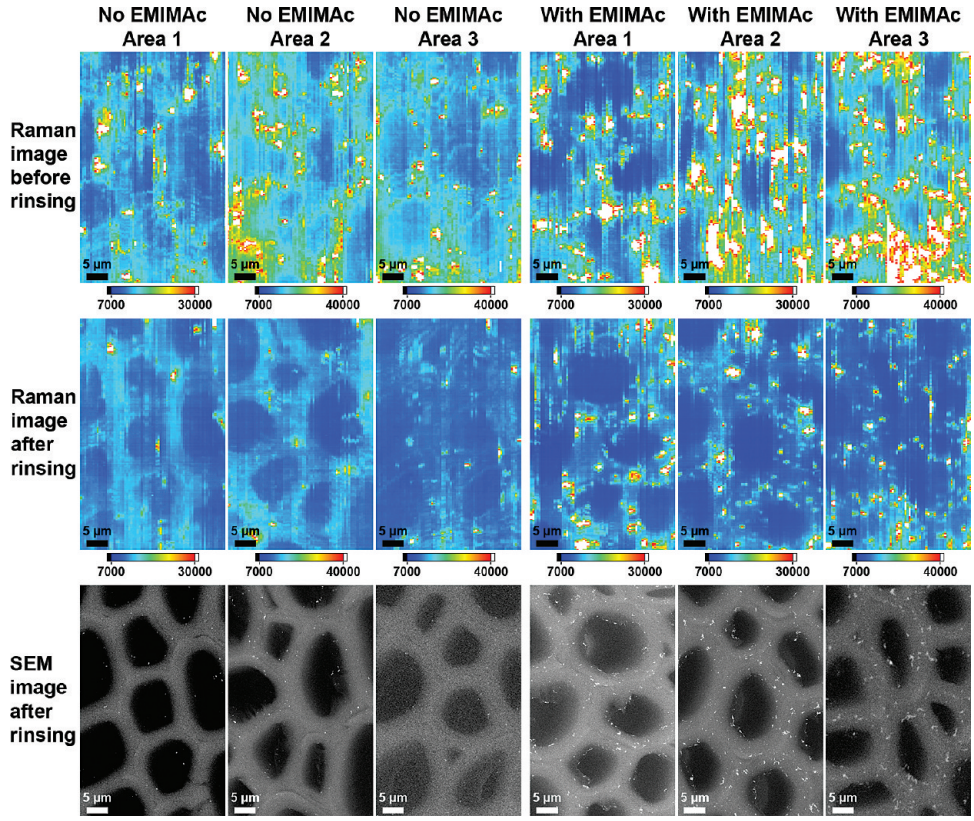

FIGURE 2. Raman and SEM images at three different areas after deposition of gold nanoparticles on the untreated wood sample (no EMIMAc) and the sample pretreated with 1-ethyl-3-methylimidazolium acetate (EMIMAc) for 3 h. Following the deposition of nanoparticles, a Raman image was collected for each position (top row). The samples were then rinsed with deionized water and Raman (middle row) and SEM (bottom row) images were collected at the same positions.

the 1120 cm^{-1} band varies from 1115 to 1128 cm^{-1}. The lignin peak around 1600 cm^{-1} was not integrated for the Raman images, due to its overlap with background signals from EMIMAc and the glass substrate. The Raman images from three different areas show that the density of hot spots is reasonably uniform across the untreated and pretreated samples. The density of hot spots on the untreated sample is comparable to the one on the pretreated sample, but no SEM images were collected for confirmation before rinsing because of the eventual sample damage. The intensity of the hot spots was found to be consistently higher on the pretreated sample, and this is partially explained by an overlap between the cellulose and EMIMAc Raman bands.

After the first series of Raman images, both samples were rinsed with deionized water at similar flow rates and left to dry overnight in air. A second series of Raman images at the same areas were collected after rinsing for direct comparison (Figure 2, middle row). Most hot spots on the untreated sample disappeared after rinsing, leaving only a few for each image covering an area of 35 × 55 μm^2. The rinsed sample pretreated with EMIMAc retained most hot spots on the Raman image. To confirm the removal of nanoparticles after rinsing, SEM images were collected from the same areas from both samples (Figure 2, bottom row). The SEM images show that most nanoparticles were removed after rinsing from the untreated sample, whereas a high density of gold nanoparticles remained on the pretreated sample. On the rinsed untreated sample, the nanoparticles are mostly isolated. A few aggregates are observed and their size is typically below five nanoparticles, the largest consisting of a dozen nanoparticles. On the rinsed pretreated sample, the nanoparticles are rarely isolated and tend to form larger aggregates. Most aggregates contain 10−30 nanoparticles. Most nanoparticles and aggregates of nanoparticles observed on the SEM images yield a hot spot with variable enhancement on their corresponding Raman images, especially for the pretreated sample with the largest aggregates. For the untreated sample with the smaller aggregates, a large number of isolated nanoparticles and small aggregates yield no hot spot on the Raman image (see area 2 of untreated sample). The larger aggregate size in the pretreated sample explains the higher intensity of the hot spots, since aggregate size affects the appearance of hot spots (34) and the nanoparticle surface plasmon resonance (35). Similarly, the intensity decrease of all hot spots in the pretreated sample after rinsing can be explained by a reduction in aggregate size. This intensity decrease can be also explained partially by the removal of some ionic liquid during the rinsing. Overall, the Raman and SEM images showed no preferential deposition of nanoparticles in the cell corners, middle lamella, or secondary cell walls.

After the second series of Raman images, but before the acquisition of SEM images, a series of Raman images at different depths from −4 to +6 μm were acquired from the area labeled Area 1 in Figure 2 for the untreated and pretreated samples (Figure 3). The depth 0 μm in Figure 3

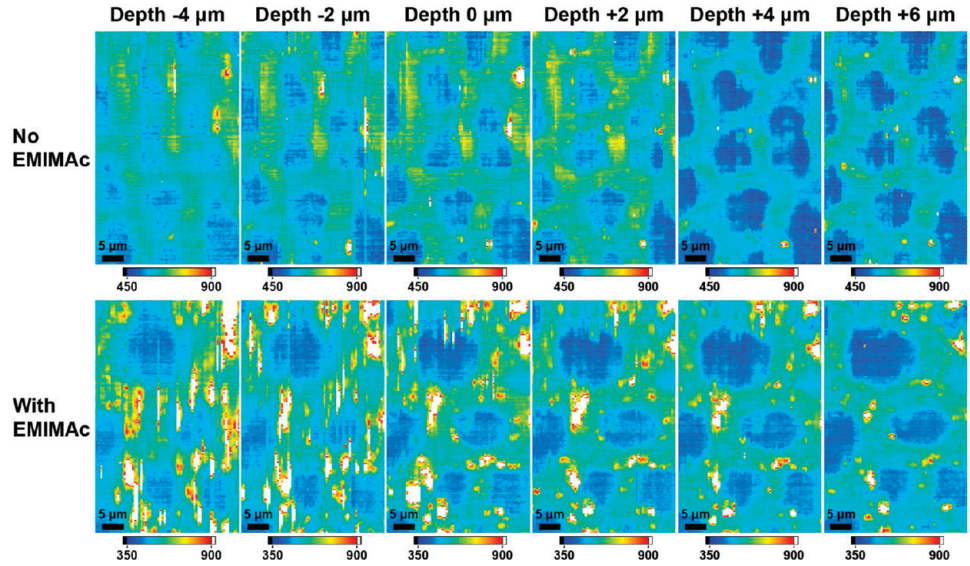

FIGURE 3. Raman images at different depths after deposition of nanoparticles and rinsing on the untreated wood sample and the sample pretreated with EMIMAc. The areas imaged correspond to those labeled area 1 in Figure 2 for each sample. The depth 0 μm corresponds to the surface of the sample.

corresponds to the surface of the sample. At this depth, the optical image of the sample is focused and the instrument was aligned so that the Raman intensity from dry wood is maximal when the optical image is focused. Positive depths correspond to a shorter distance between the objective and the sample, meaning the laser line is focused inside the sample. The cell walls aligned along the vertical direction of the images exhibit a consistently higher Raman intensity that those aligned along the horizontal direction. This is attributed to the incident laser being naturally polarized along the vertical direction of the image and the orientation of the cellulose fibrils. Indeed, the cellulose fibrils in the secondary cell wall layer S2 (closer to the lumen, and generally the thickest) were found to be aligned along the grain of the wood, while those of the secondary cell wall layer S1 (closest to the middle lamella) form an angle greater than 45° with the direction along the grain of the wood (24, 25). The intensity of all hot spots varies as the depth is changed. Most hot spots in the pretreated sample are still visible in the image collected at a depth of 6 μm, while only a few are still visible at the same depth in the untreated sample. At this point, it is important to note that the laser line focusing enabled the collection of Raman images at a reasonable exposure time (total of less than 30 min for each image) and the accurate registry (32, 36).

To determine whether the gold nanoparticles are adsorbed at the sample surface or incorporated deep inside the sample, the intensity of six and twelve hot spots was measured as a function of depth for the untreated sample (Figure 4) and pretreated sample (Figure 5), respectively. Included in this study are all hot spots that could be tracked across the images at different depths. A few hot spots (less than 5% of the total number) were excluded because their intensity depth profiles exhibit two distinct maxima. A few large aggregates contain nanoparticles stacked on top of others, and so it is unclear if the maxima correspond to hot spots from the same nanoparticles or multiple nanoparticles.

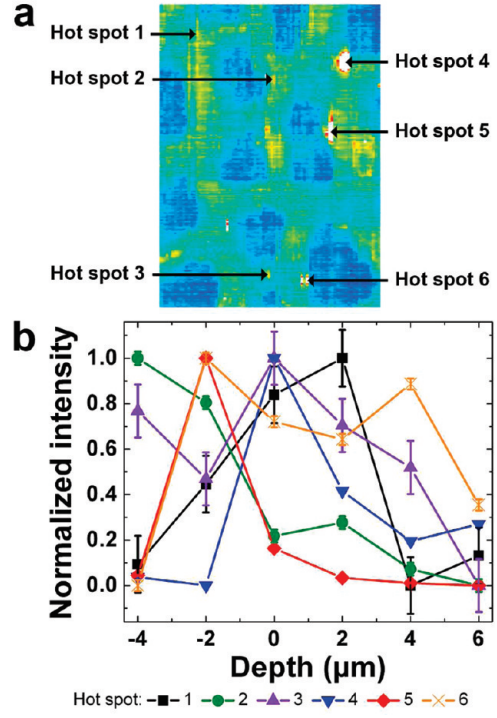

FIGURE 4. Raman intensity depth profile of six hot spots for the untreated wood sample designated in (a) the Raman image at depth 0 μm by arrows.

The intensity depth profiles presented in Figures 4 and 5 have full width at half-maximum ranging from 2 μm for the most intense hot spots to 4 μm for the less intense hot spots. The depth resolution is sufficient to determine whether the particle is at the surface or incorporated inside the sample.

For the untreated sample, the intensity of all hot spots reaches a maximum at a depth around 0 μm or at a negative depth. The area under the curve for all depth profiles is dominated by contributions from negative depths. The electromagnetic field enhancement around the nanoparticles leading to SERS activity is local, only noticeable within

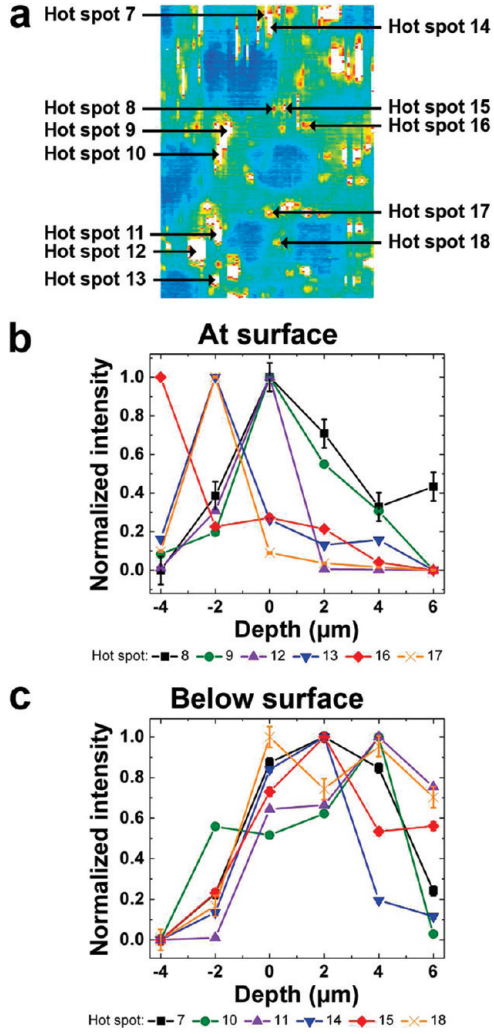

FIGURE 5. Raman intensity depth profile of 12 hot spots for the pretreated wood sample designated in (a) the Raman image at depth 0 μm by arrows. The intensity profiles for the hot spots 8, 9, 12, 13, 16, and 17 shown in (b) exhibit a maximum at negative depths, meaning that the corresponding nanoparticles are at the sample surface. In contrast, the intensity profiles for the hot spots 7, 10, 11, 14, 15, and 18 shown in (c) exhibit a maximum at positive depths, meaning that the corresponding nanoparticles are incorporated inside the sample.

a distance of 10 nm from the nanoparticles (37). Therefore, the nanoparticles producing these hot spots are all at the surface of the sample. As for the pretreated sample, the intensity depth profiles of six hot spots from nanoparticles at the surface and six others from nanoparticles incorporated inside the sample are shown in panels b and c in Figure 5, respectively. The hot spots 10 and 11 reach their maximum intensity at a depth of 4 μm. This depth is 40 times the diameter of the nanoparticle. Nanoparticles may be embedded much deeper into the cell walls, but the Raman signal decreases significantly at depths larger than 6 μm, making their detection and location difficult. Smaller nanoparticles are expected to penetrate even deeper into the wood structure. From the data shown in Figures 3 and 5, it is estimated that, for this area, at least 25% of nanoparticles are below the surface. It is noted that the nanoparticles highlighted in Figures 4 and 5 are in the cell walls and middle lamella, and not adsorbed on the side of the lumen. The 4 μm depth mentioned above corresponds to an incorporation of the nanoparticle from the top inward. Optical images of the cell walls at other locations revealed pits with sizes smaller than 2 μm, which is much smaller than the smallest cells shown in Figure 1c. Figure 1c shows that the smallest cells are completely shut by the expansion of the wood due to EMIMAc pretreatment. The much smaller pits are also expected to be completely shut during the EMIMAc pretreatment, denying the access to nanoparticles. Figures 2 and 3 from the untreated sample show no nanoparticles embedded inside the sample after rinsing. This means that nanoparticles cannot be trapped inside the pits even when the pits are open in the untreated sample. The swollen and shut pits in the pretreated sample are expected to be even more effective in denying access to nanoparticles.

The incorporation of nanoparticles in the pretreated sample is attributed to the expansion of wood cells upon exposure to EMIMAc. Ionic liquids are known for their ability to disrupt the three-dimensional hydrogen-bonding network in cellulose and wood, allowing them to diffuse inside wood cells (3, 17, 20). The overall expansion and disruption of hydrogen bonding increased the distance between polymer chains inside the wood structure, paving the way for the incorporation of nanoparticles. The contraction of the cell walls after rinsing ensured that the nanoparticles would remain on the sample even after rinsing. As for the untreated sample, water tends to adsorb on cellulose and hemicellulose by forming hydrogen bonds (38). The more limited expansion of untreated wood samples and the formation of hydrogen bonds between water and wood cells restrict the access of nanoparticles inside the sample. The nanoparticles at the surface of the untreated sample are only weakly adsorbed and can be easily washed away upon rinsing.

CONCLUSIONS

A microtome section of poplar wood was swollen by a 3 h ionic liquid (1-ethyl-3-methylimidazolium acetate) pretreatment. The pretreated sample was then exposed to an aqueous suspension of gold nanoparticles of 100 nm diameter that resulted in the sample contraction and the deposition of nanoparticles as confirmed by Raman images. After rinsing with water, SEM and Raman images of the same areas show that most nanoparticles remained on the sample. Raman images at different depths reveal that at least 25% of deposited nanoparticles were incorporated into the wood sample, at depths up to 4 μm. Control experiments on untreated wood samples resulted in the deposition of nanoparticles only at the surface and most nanoparticles were removed upon rinsing. Quantitative X-ray fluorescence microanalyses indicate that the majority of nanoparticle incorporation occurs after an ionic liquid pretreatment shorter than 1 h. This particle incorporation process based on the swelling/contraction of the wood and the disruption of its hydrogen-bond network enables isotope tracing, the development of new sensing and imaging capabilities and pretreatments.

Acknowledgment. This study was funded by a Laboratory Directed Research and Development grant from Los Alamos

National Laboratory (20080001DR). The authors acknowledge Dr. Paul Langan (Los Alamos National Laboratory) and Prof. Constance Schall (University of Toledo) for useful discussions.

Supporting Information Available: Representative Raman spectra of dehydrated wood, rehydrated wood, pure EMIMAc, wood pretreated with EMIMAc, wood pretreated with EMIMAc and rinsed, and the glass substrate (PDF). This material is available free of charge via the Internet at http://pubs.acs.org.

REFERENCES AND NOTES

(1) Banerjee, S.; Mudliar, S.; Sen, R.; Giri, B.; Satpute, D.; Chakrabarti, T.; Pandey, R. A. *Biofuels, Bioprod. Biorefin.* **2010**, *4*, 77–93.
(2) Huber, G. W.; Iborra, S.; Corma, A. *Chem. Rev.* **2006**, *106*, 4044–4098.
(3) Kilpeläinen, I.; Xie, H.; King, A.; Granstrom, M.; Heikkinen, S.; Argyropoulos, D. S. *J. Agric. Food Chem.* **2007**, *55*, 9142–9148.
(4) Pienkos, P. T.; Zhang, M. *Cellulose* **2009**, *16*, 743–762.
(5) von Sivers, M.; Zacchi, G. *Bioresour. Technol.* **1995**, *51*, 43–52.
(6) Yang, B.; Wyman, C. E. *Biofuels, Bioprod. Biorefin.* **2008**, *2*, 26–40.
(7) Mackie, K. L.; Brownell, H. H.; West, K. L.; Saddler, J. N. *J. Wood Chem. Technol.* **1985**, *5*, 405–425.
(8) Bjerre, A. B.; Olesen, A. B.; Fernqvist, T.; Plöger, A.; Schmidt, A. S. *Biotechnol. Bioeng.* **1996**, *49*, 568–577.
(9) Pinkert, A.; Marsh, K. N.; Pang, S.; Staiger, M. P. *Chem. Rev.* **2009**, *109*, 6712–6728.
(10) Dadi, A. P.; Varanasi, S.; Schall, C. A. *Biotechnol. Bioeng.* **2006**, *95*, 904–910.
(11) Dadi, A. P.; Schall, C. A.; Varanasi, S. *Appl. Biochem. Biotechnol.* **2007**, *136–140*, 407–422.
(12) Kosan, B.; Michels, C.; Meister, F. *Cellulose* **2008**, *15*, 59–66.
(13) Lee, S. H.; Doherty, T. V.; Linhardt, R. J.; Dordick, J. S. *Biotechnol. Bioeng.* **2009**, *102*, 1368–1376.
(14) Tan, S. S. Y.; MacFarlane, D. R.; Upfal, J.; Edye, L. A.; Doherty, W. O. S.; Patti, A. F.; Pringle, J. M.; Scotta, J. L. *Green Chem.* **2009**, *11*, 339–345.
(15) Pu, Y.; Jiang, N.; Ragauskas, A. J. *J. Wood Chem. Technol.* **2007**, *27*, 23–33.
(16) Singh, S.; Simmons, B. A.; Vogel, K. P. *Biotechnol. Bioeng.* **2009**, *104*, 68–75.
(17) Xie, H.; King, A.; Kilpelainen, I.; Granstrom, M.; Argyropoulos, D. S. *Biomacromolecules* **2007**, *8*, 3740–3748.
(18) Fort, D. A.; Remsing, R. C.; Swatloski, R. P.; Moyna, P.; Moyna, G.; Rogers, R. D. *Green Chem.* **2007**, *9*, 63–69.
(19) Sun, N.; Rahman, M.; Qin, Y.; Maxim, M. L.; Rodríguez, H.; Rogers, R. D. *Green Chem.* **2009**, *11*, 646–655.
(20) Swatloski, R. P.; Spear, S. K.; Holbrey, J. D.; Rogers, R. D. *J. Am. Chem. Soc.* **2002**, *124*, 4974–4975.
(21) Pottkämper, J.; Barthen, P.; Ilmberger, N.; Schwaneberg, U.; Schenk, A.; Schulte, M.; Ignatiev, N.; Streit, W. R. *Green Chem.* **2009**, *11*, 957–965.
(22) Holtzapple, M. T.; Humphrey, A. E.; Taylor, J. D. *Biotechnol. Bioeng.* **1989**, *33*, 207–210.
(23) Zhu, J. Y.; Wang, G. S.; Pan, X. J.; Gleisner, R. *Chem. Eng. Sci.* **2009**, *64*, 474–485.
(24) Agarwal, U. P. *Planta* **2006**, *224*, 1141–1153.
(25) Gierlinger, N.; Schwanninger, M. *Spectroscopy* **2007**, *21*, 69–89.
(26) Schenzel, K.; Almlöf, H.; Germgård, U. *Cellulose* **2009**, *16*, 407–415.
(27) Agarwal, U. P.; Reiner, R. S. *J. Raman Spectrosc.* **2009**, *40*, 1527–1534.
(28) Trindade, T.; O'Brien, P.; Pickett, N. L. *Chem. Mater.* **2001**, *13*, 3843–3858.
(29) Jain, P. K.; Lee, K. S.; El-Sayed, I. H.; El-Sayed, M. A. *J. Phys. Chem. B* **2006**, *110*, 7238–7248.
(30) Gupta, A. K.; Gupta, M. *Biomaterials* **2005**, *26*, 3995–4021.
(31) Sun, B.; Marx, E.; Greenham, N. C. *Nano Lett.* **2003**, *3*, 961–963.
(32) Nowak-Lovato, K. L.; Rector, K. D. *Appl. Spectrosc.* **2009**, *63*, 387–395.
(33) Misra, M. K.; Ragland, K. W.; Baker, A. J. *Biomass Bioenergy* **1993**, *4*, 103–116.
(34) Khan, I.; Cunningham, D.; Graham, D.; McComb, D. W.; Smith, W. E. *J. Phys. Chem. B* **2005**, *109*, 3454–3459.
(35) Basu, S.; Pande, S.; Jana, S.; Bolisetty, S.; Pal, T. *Langmuir* **2008**, *24*, 5562–5568.
(36) De Grauw, C. J.; Otto, C.; Greve, J. *Appl. Spectrosc.* **1997**, *51*, 1607–1612.
(37) Pettinger, B.; Domke, K. F.; Zhang, D.; Schuster, R.; Ertl, G. *Phys. Rev. B* **2007**, *76*, 113409.
(38) Olsson, A.-M.; Salmén, L. *Carbohydr. Res.* **2004**, *339*, 813–818.

AM100371Q